MDPI

Article

Thermodynamic Optimization of Ammonia Decomposition Solar Heat Absorption System Based on Membrane Reactor

Tianchao Xie, Shaojun Xia * and Qinglong Jin

College of Power Engineering, Naval University of Engineering, Wuhan 430033, China;
weitonghe@stu.xaut.edu.cn (T.X.); 18404133@masu.edu.cn (Q.J.)
* Correspondence: 2020281050888@whu.edu.cn; Tel.: +86-27-8365-0532

Abstract: In this paper, an ammonia decomposition membrane reactor is applied to a solar heat absorption system, and thermodynamic optimization is carried out according to the usage scenarios. First, a model of an ammonia decomposition solar heat absorption system based on the membrane reactor is established by using finite time thermodynamics (FTT) theory. Then, the three-objective optimization with and the four-objective optimization without the constraint of the given heat absorption rate are carried out by using the NSGA-II algorithm. Finally, the optimized performance objectives and the corresponding design parameters are obtained by using the TOPSIS decision method. Compared with the reference system, the TOPSIS optimal solution for the three-objective optimization can reduce the entropy generation rate by 4.8% and increase the thermal efficiency and energy conversion rate by 1.5% and 1.4%, respectively. The optimal solution for the four-objective optimization can reduce the heat absorption rate, entropy generation rate, and energy conversion rate by 15.5%, 14%, and 8.7%, respectively, and improve the thermal efficiency by 15.7%. The results of this paper are useful for the theoretical study and engineering application of ammonia solar heat absorption systems based on membrane reactors.

Keywords: ammonia decomposition; membrane reactor; solar heat absorption system; multi-objective optimization; finite-time thermodynamics

1. Introduction

Ammonia has a large volume energy density, and its decomposition and synthesis reactions have the advantages of no side reaction, good reversibility, and remarkable heat absorption and release effect [1–3], which make ammonia a well-suited working medium for solar thermochemical energy storage. Meanwhile, ammonia is a high-density hydrogen carrier and can be used to produce hydrogen with zero carbon emissions. Therefore, ammonia has broad development prospects in both thermochemical energy storage and hydrogen energy fields.

In the engineering and experimental research on ammonia energy storage systems, Lovegrove [4] used an electrically heated ammonia decomposition reactor to conduct experiments and achieved a heat absorption rate of 2 kW when the reaction temperature and pressure were 720 °C and 17 MPa, respectively. The activation energy and pre-exponential factor for the ammonia decomposition kinetic model were also obtained in Ref. [4]. Luzzi [5,6] used a 20 m² parabolic dish solar collector to heat an ammonia decomposition reactor under the light intensities of 500–1116 W/m², and showed that the ammonia conversion rate was 38.4–84.6% and the peak heat absorption rate was 2.5 kW. Meanwhile, 58% solar energy was absorbed by the reactants, of which 82–88% was converted to chemical energy. In 1999, the Australian National University built an experimental solar thermal power generation plant using a 20 m² dish solar collector. Under the support from an energy storage system taking ammonia as the working fluid, the plant could achieve 24 h stable power generation [7] with a power capacity of 1 kW. Subsequently, Dunn [8,9] optimized the design of the dish

collector to achieve a 49% energy efficiency at a 55-degree solar elevation angle and showed that 33% of the solar energy was converted into chemical energy.

The application of a hydrogen-permeable palladium membrane [10–12] can effectively improve the reactor performance. In the performance simulation of ammonia decomposition membrane reactors, Itoh et al. [13] found that the palladium membrane reactor could permeate up to 60% of the generated hydrogen and the ammonia conversion rate was 15% higher than traditional ones. At the same time, thinner palladium membranes are beneficial to further enhance the reactor performance. Abashar et al. [14,15] investigated the effect of feed point distribution along the reactor axis on the membrane reactor performance and found that the optimal ammonia injection point distribution could reduce the reactor length required for complete ammonia decomposition by 75%. Wang et al. [16] analyzed the effects of reaction temperature, tube length, and permeation zone pressure on the exergy efficiency and conversion rate of a constant-temperature ammonia decomposition membrane reactor. They calculated the solar conversion rate and coal saving rate by converting the heat absorption of the reactor to solar radiation. Cechetto et al. [17] achieved complete decomposition of ammonia and separated 86% hydrogen by using a membrane reactor at 425 °C. They found that the inlet flow rate and reaction pressure of ammonia did not significantly affect the conversion rate. Sitar et al. [18] found that the addition of zeolite to the membrane reactor could effectively enhance the permeability of the palladium membrane and reduce the impurities in the permeated hydrogen. Cerrillo et al. [19] used hydrogen produced by ammonia decomposition to supply energy to the membrane reactor at a high pressure of 350 bar, and the energy utilization efficiency of hydrogen reached 75%. Existing studies mainly focused on improving hydrogen yield and ammonia conversion rate and were mainly on a single reactor. It is very necessary to apply finite-time thermodynamics (FTT) [20–23] to optimize multiple performance indicators such as heat absorption rate, reversibility, and energy efficiency at system and process levels.

FTT [20–23] focuses on the performance optimization of irreversible processes and equipment under finite-time or finite-size constraints. After more than four decades of development, FTT has achieved many results in the analysis and optimization of engineering chemical reactors. Badescu [24] studied an ammonia decomposition filled-bed reactor in the steady state. The maximum ammonia conversion rate and minimum heat consumption at a fixed conversion rate were taken as objectives, and the reactor temperature distribution was optimized. Xie et al. [25] established a model of the ammonia decomposition solar heat absorption system based on a membrane reactor and analyzed the effects of ammonia flow rate, reactor diameter, and light intensity on system performance indicators such as entropy generation rate, thermal efficiency, and heat absorption rate. Kong et al. [26–28] optimized the temperature distribution of the HI decomposition membrane reactor with the objectives of highest HI conversion rate, maximum hydrogen yield, and minimum entropy generation rate. In addition, FTT has shown broad prospects on the analysis and optimization of reactors for ammonia synthesis [29], sulfuric acid decomposition [30,31], methane steam reforming [32,33], methanol synthesis [34,35] and so on.

In summary, in the energy storage application of the ammonia decomposition membrane reactor, Ref. [16] took a thermostatic reactor as an object and converted the heat absorption to solar radiation to calculate the energy conversion rate and coal saving rate. This situation still has a certain gap with the engineering practice. In the thermodynamic analysis of the ammonia decomposition heat absorption system, Ref. [25] established a model of the ammonia decomposition heat absorption system heated by real sunlight, and analyzed the effect of parameters on thermal efficiency, endothermic rate, and entropy generation rate. However, the thermodynamic optimization of the system is still lacking. Based on Ref. [25] and the theory of FTT, the geometry and operating parameters of the ammonia decomposition solar heat absorption system are optimized using the NSGA-II algorithm in this paper.

2. Physical Model

A schematic diagram of the ammonia decomposition solar heat absorption system based on the membrane reactor is shown in Figure 1. In order to more truly reflect the influence of the actual light intensity on system performances, a trough solar collector is used in the system to concentrate sunlight on the reactor outer wall to provide energy for ammonia decomposition. After trial calculation, the reactor outlet temperature of mixed gas can reach 700 K. Adding a regenerator to the system can preheat the inlet ammonia of the reactor, improve system performances, and shorten the length of the reactor. As the reaction flow process is accompanied by a pressure drop, a compressor is added at the reactor outlet to pressurize the outlet gas to 7 bar.
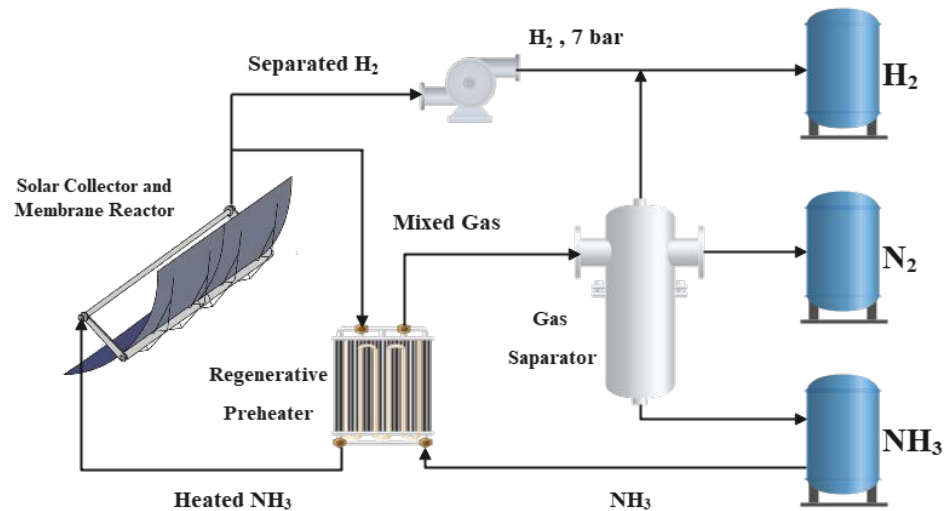

Figure 1. Schematic diagram of ammonia decomposition solar heat absorption system [25]. Reprinted/adapted with permission from Ref. [25]. 2022, Tianchao Xie.

2.1. Solar Collector Model

In this paper, the ET-100 trough collector is used to concentrate the solar energy to the reactor wall as a boundary condition. The main parameters of the ET-100 collector are listed in Table 1.

Table 1. Main design parameters of ET-100 collector [36].

Parameter Name	Symbol	Value
Opening width	K_s	5.76 m
Condenser reflectivity	η_s	94%
Glass outer tube transmittance	δ_s	96%
Radiation absorption rate of reactor	ε_s	95%
Reactor surface emissivity	ρ_s	14%

Reprinted/adapted with permission from Ref. [36]. 2009, Yaxuan Xiong.

The solar rays are reflected by the condenser, pass through the outer glass, and irradiate the reactor surface. Therefore, the solar radiation boundary condition of the reactor is [25]:

$$P_s = P_{sun} K_s \eta_s \delta_s \varepsilon_s \tag{1}$$

where P_{sun} is the average radiant power density of the sun shining on the ground, in W/m^2; K_s is the condenser reflectivity of the condenser reflector; δ_s is the light transmittance of the reactor outer glass tube; ε_s is the radiation absorption rate of the reactor; P_s is the energy power finally absorbed by the outer wall of the reactor from solar radiation in W/m.

2.2. Ammonia Decomposition Membrane Reactor Model

The hydrogen-permeable membrane can filter the generated hydrogen from the reaction system, to push the chemical reaction balance to shift to the positive reaction direction and improve the reactor performance. Figure 2 is the schematic diagram of the ammonia decomposition membrane reactor.
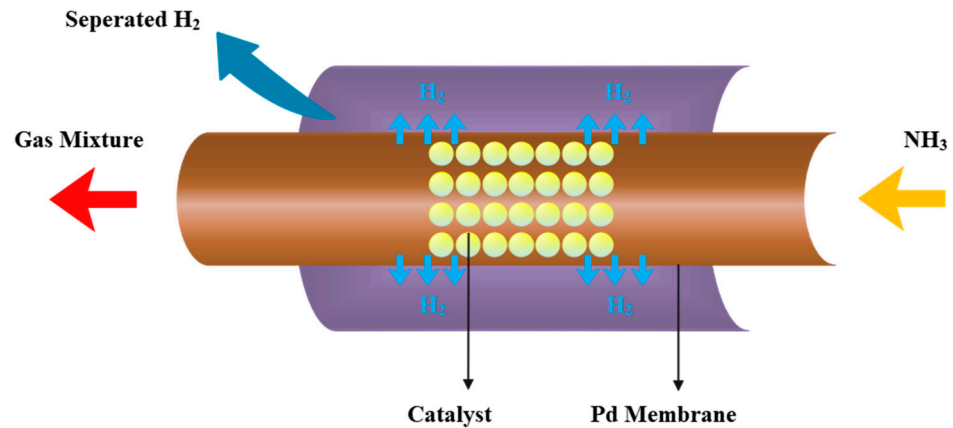

Figure 2. Schematic diagram of an ammonia decomposition membrane reactor [25]. Reprinted/adapted with permission from Ref. [25]. 2022, Tianchao Xie.

According to reference parameters of the system, the reactor length can reach 10 m, while the reactor diameter is only about 7 cm, a difference of more than 100 times, so the reactor is idealized as a one-dimensional model. The gas composition and temperature distribution in the cross-section are considered to be uniform, and the nonuniformity of the heat flow distribution along the outer wall of the reactor caused by the trough concentrator is ignored. After preheating, ammonia gas flows into the reactor from the right side, the temperature rises under the heating of solar energy, and then the decomposition reaction starts. After the partial pressure of hydrogen in the reaction zone exceeds the permeation zone pressure, the permeation process begins. The hydrogen will pass through the palladium membrane into the permeation zone and is pumped out by the compressor.

2.2.1. Reaction Kinetic Equation

The ammonia decomposition reaction kinetic equation fits the Temkin–Pyzhev mechanism model [37]:

$$r_A = \frac{K_b}{K_c{}^{2\alpha}} \left[K_a{}^2 p_N \left(\frac{p_H{}^3}{p_A{}^2} \right)^\alpha - \left(\frac{p_A{}^2}{p_H{}^3} \right)^{1-\alpha} \right] \tag{2}$$

where p_i is the partial pressure, in bar, and i represents the component (A = ammonia, N = nitrogen, and H = hydrogen); r_A is the decomposition reaction speed, in mol/(m^3 s); α is a constant related to the nitrogen decomposition state on the catalyst surface, which ranges from 0 to 1 and is taken as 0.75 here [25]. K_a is the equilibrium constant of the ammonia decomposition reaction, and K_b and K_c represent the intrinsic reaction rate constants for the forward and reverse reactions [25,37].

2.2.2. Conservation Equations

For the reactor, the conservation equations consist of three parts: energy conservation, momentum conservation, and mass conservation.

The reactor operates in a steady state, the input energy of the reactor micro-element is the solar energy obtained from the reactor wall, and this energy is dissipated from three paths: the ammonia decomposition endothermic reaction, and the radiative and convective heat dissipation of the reactor. Therefore, under the constraint of the first law of

thermodynamics, the temperature change of mixed gas in the micro-element can be used to express the energy conservation:

$$\frac{\mathrm{d}T}{\mathrm{d}z} = \frac{P_s - A_c(1-\varepsilon_p)r_A\Delta_r H - H_h - H_e}{\sum_k F_k C_{p,k}} \tag{3}$$

where P_s is the solar energy absorbed by the outer wall, which is calculated in Equation (1), in W/m; A_c is the inner cross-sectional area of the reactor; ε_p is the bed porosity in the reaction zone; r_A is the ammonia decomposition reaction speed, in mol/(m^3 s); $\Delta_r H$ is the molar enthalpy of formation of ammonia, in J/mol; $C_{p,k}$ is the constant-pressure heat capacity, where the subscript k represents different substances; F_k is the flow rate of component k, in mol/s; H_h is the convective heat loss of the reactor, in W; H_e is the radiant heat loss, in W.

The collector tube equipped with the trough collector usually has a vacuum glass layer on the outside, which can greatly weaken the convection heat transfer and improve the thermal efficiency. In the model of this paper, the glass cavity is the permeation area, and the permeated hydrogen is pumped out of the reactor through this area, so the convective heat dissipation of the reactor cannot be ignored. In order to simplify the calculation process, the convective heat transfer coefficient in this paper is based on $h_0 = 10$ W/(m^2 K), and the actual heat transfer coefficient is proportional to the permeation zone pressure. The convection heat transfer in Equation (3) is obtained as [23]:

$$H_h = \frac{P_P}{P_0} h_0 \pi D_1 (T_a - 550) \tag{4}$$

where p_0 is the standard atmospheric pressure; T_a is the outer wall temperature, in K.

The radiant heat loss of reactor can be calculated by Equation (3):

$$H_e = \rho_s \sigma T_a^4 \tag{5}$$

where ρ_s is reactor surface emissivity; σ is the Stefan–Boltzmann constant of radiation heat dissipation, which is 5.67 W/(m^{2}K^4).

The trial calculation shows that the Re number in the reactor ranges from 3000 to 16,000, so the Hicks pressure drop equation is suitable for this situation. We use the Hicks equation to express the momentum conservation [38]:

$$\frac{\mathrm{d}p}{\mathrm{d}z} = -6.8 \frac{(1-\varepsilon_p)^{1.2}}{\varepsilon_p^3} \mathrm{Re}^{-0.2} \frac{\rho_m c_m^2}{D_p} \tag{6}$$

where ε_p is the bed porosity; ρ_m is the average density of the reaction system, in kg/m^3; c_m is the flow rate of mixed gas in the reaction zone, in m/s; D_p is the catalyst particle diameter, in m.

We use the change in hydrogen flow rate to describe the mass conservation equation:

$$\frac{\mathrm{d}F_{H_2}}{\mathrm{d}z} = A_c(1-\varepsilon_p)r_{H_2} - J_{H_2} \tag{7}$$

where the hydrogen permeation is [16]:

$$J_{H_2} = \frac{k(p_{H_2}^n - p_P^n)}{d\mathrm{M}} \tag{8}$$

$$k = 3.21 \times 10^{-8} \exp\left(-\frac{13140}{RT_a}\right) \tag{9}$$

where R is the universal gas constant; P_{H_2} is the partial pressure of hydrogen in the reaction zone, in Pa; d_M is the palladium film thickness, in m; n is an exponent that ranges from 0.5 to 1, and it is equal to 0.62 in this paper.

2.3. Compressor Model

Due to the pressure drop, the inlet pressure of the ammonia decomposition endothermic system is 7 bar, while the outlet pressure of the reactor is reduced to about 4 bar. In addition, the permeation zone pressure is set at 0.1–1 bar. For the complete assessment of the energy consumption of the entire system, a compressor is added at the reactor outlet to pressurize the gas to 7 bar. Assuming that the compression process is adiabatic compression, there are:

$$p^{K-1}V^{K} = C \tag{10}$$

where C is a constant; K is the adiabatic index.

Combining Equation (10) with the ideal gas state equation, the relationship between the inlet and outlet gas pressure and temperature in the reversible adiabatic compression process is:

$$\frac{T_{\mathrm{r}}}{T_{\mathrm{in}}} = \left(\frac{p_{\mathrm{out}}}{p_{\mathrm{in}}}\right)^{\frac{\gamma-1}{\gamma}} \tag{11}$$

where T_{in} and p_{in} are the temperature and pressure at the inlet of the compressor, respectively; p_{out} is the compressor outlet pressure. Based on this, the outlet working fluid temperature T_{r} of reversible compression can be calculated.

The compressor used in this paper is irreversible adiabatic compression, and the compression efficiency is 0.7. The definition of the compression efficiency is:

$$\frac{h_{\mathrm{r}} - h_{\mathrm{in}}}{h_{\mathrm{ir}} - h_{\mathrm{in}}} = 0.7 \tag{12}$$

where h_{in} is the inlet enthalpy of the compressor working fluid, and h_{r} and h_{ir} are the outlet enthalpies corresponding to the reversible adiabatic compression and the irreversible adiabatic compression, respectively. h_{r} is obtained from the outlet working fluid temperature T_{r} of reversible adiabatic compression; the irreversible adiabatic compression outlet temperature T_{ir} can be calculated using h_{ir}.

2.4. Performance Index

2.4.1. Heat Absorption Rate

The total energy absorbed by the reactor is defined as the heat absorption rate (*HAR*), which is an important performance index of the heat storage system and characterizes its ability to absorb solar energy. As the system is in a steady state, the heat absorption rate is equal to the heat reaction gas obtained from the outer surface [23]:

$$HAR = \int_{0}^{L} 2\pi R_1 h(T_a - T)\mathrm{d}z \tag{13}$$

where R_1 is the outer radius, in m; h is the heat transfer coefficient of the reactor wall, in W/(m^2 K); T_a and T are the temperature of the reactor wall and reaction system, in K.

2.4.2. Entropy Generation Rate

The system is composed of a membrane reactor, a regenerator, and two compressors. Thus, the entropy generation rate of the system is mainly composed of three parts:

$$S_{\mathrm{G,SUM}} = S_{\mathrm{G,R}} + S_{\mathrm{G,E}} + S_{\mathrm{G,C}} \tag{14}$$

$S_{\mathrm{G,R}}$, $S_{\mathrm{G,E}}$, and $S_{\mathrm{G,C}}$ are the entropy generation rates produced from the reactor, regenerator, and compressors, respectively.

$S_{\mathrm{G,R}}$ can be calculated by integrating the local total entropy generation rate (σ_{R}) along the reactor length. At the same time, σ_{R} is composed of three parts: ammonia

decomposition reaction, heat transfer between reactor wall and reaction gas, and pressure drops during the flow [25]:

$$\sigma_R = \sigma_r + \sigma_h + \sigma_p \tag{15}$$

For the regenerator, as it is adiabatic and the inlet and outlet states of ammonia (cold working fluid) and the gas mixture out from the reactor (hot working fluid) remain unchanged, the entropy generation rate of the regenerator ($S_{G,E}$) can be calculated by the inlet and outlet entropy changes of the regenerator [25]:

$$S_{G,HE} = \int_{T_0}^{T_1} \frac{C_{p,NH3}}{T} dT + \int_{T_2}^{T_3} \frac{C_{p,mix}}{T} dT \tag{16}$$

where T_0 and T_1 are the ammonia temperatures at the inlet and outlet of the regenerator, respectively, in K; T_2 and T_3 are the temperatures of the mixed gas at the inlet and outlet of the regenerator, respectively, in K.

The compressor entropy generation rate ($S_{G,C}$) is calculated as follows [25]:

$$S_{G,P} = \sum_k F_k \int_{Tr}^{Tir} \frac{C_{p,k}}{T} dT \tag{17}$$

2.4.3. Thermal Efficiency

In the operation of the system, not only the solar energy, but also the power consumption is involved. The power consumption is caused by compressors, the lower permeation pressure may promote the reaction and increase the heat absorption rate, but it may lead to a larger power consumption. Therefore, the analysis of the first law efficiency is necessary for the system.

The thermal efficiency of the heat absorption system is equal to the ratio of the solar energy absorbed by the membrane reactor to the total energy consumption including solar energy and power consumption [25]:

$$\eta_{sys} = \frac{HAR}{W_{SUN} + W_C} \tag{18}$$

where HAR is the solar energy the reaction system obtains from the reactor wall, W_C is the electric power consumed by compressors, and W_{SUN} is the total solar energy put into the system.

The power of the compressor is equal to the enthalpy difference between the outlet and inlet of the irreversible adiabatic compression process:

$$W_C = h_{ir} - h_{in} \tag{19}$$

where h_{ir} and h_{in} are the outlet and inlet enthalpies of the working fluid of irreversible adiabatic compression.

2.4.4. Energy Conversion Rate

The energy absorbed by the reactor is mainly used in two parts, one part is converted into chemical energy, and the other one is converted into heat to increase the temperature of the gas. As a thermochemical energy storage system, we are more concerned about the proportion of the system that finally converts solar energy into chemical energy. Therefore, the energy conversion rate is calculated by the ratio of the chemical reaction of heat absorption to the amount of solar radiation:

$$\eta_{eng} = \frac{\int_0^L A_c(1 - \varepsilon_p) r_A \Delta_r H dz}{W_{SUN}} \tag{20}$$

3. Optimization Problems

The second-generation nondominated solution sorting genetic algorithm (NSGA-II) [39,40] proposes a fast nondominated sorting algorithm and introduces an elite strategy, which greatly improves the running speed and convergence. All these make NSGA-II one of the most popular multi-objective optimization algorithms. Based on the performance analysis in Ref. [25], the NSGA-II is utilized to optimize the ammonia flow rate, ammonia preheat end-state temperature, permeation zone pressure, and the radius and length of the reactor with the objectives of maximum *HAR*, minimum $S_{G,SUM}$, maximum η_{sys}, and maximum η_{eng}. The technique for Order Preference by Similarity to an Ideal Solution (TOPSIS) [41,42] is a decision-making method that sorts according to the closeness of the evaluation object to the idealized goal, and selects the best point. Finally, the TOPSIS decision method is used to select one optimal solution from the Pareto Front.

The mathematical description of the optimization problem is:

$$\text{Min}(-HAR, S_G, -\eta_{sys}, -\eta_{eng}) \tag{21}$$

$$s.t. \begin{cases} 400\,\text{K} \le T_c \le 600\,\text{K} \\ 0.3\,\text{mol/s} \le N_A \le 1\,\text{mol/s} \\ 2.8\,\text{cm} \le R_1 \le 3.8\,\text{cm} \\ 7\,\text{m} \le L \le 13\,\text{m} \end{cases} \tag{22}$$

Heat absorption rate is the core performance index of the ammonia decomposition endothermic system. Based on the four-objective optimization problem shown in Equations (21) and (22), this paper also obtains the standard values of heat absorption rate under different lighting conditions and carries out the three-objective optimization under this constraint.

4. Numerical Example and Result Analysis

4.1. Performance of the Reference Reactor

The simulation is performed under reference values. Figure 3 shows the variations in each component's flow rate, and Figure 4 shows the variations in the reactor wall temperature, reaction gas temperatures, and σ_R along the reactor length when the ground light intensity is 800 W/m^2.
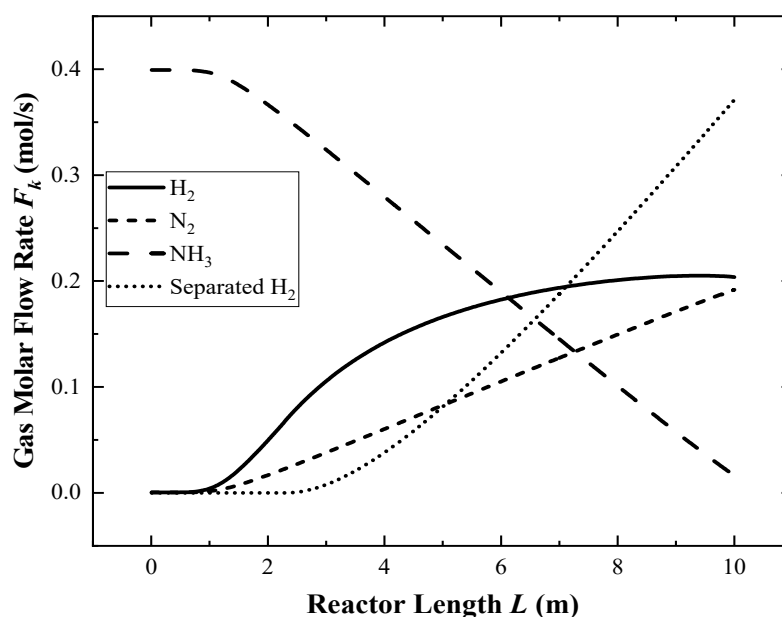

Figure 3. The distributions of each component flow rate along the reactor.
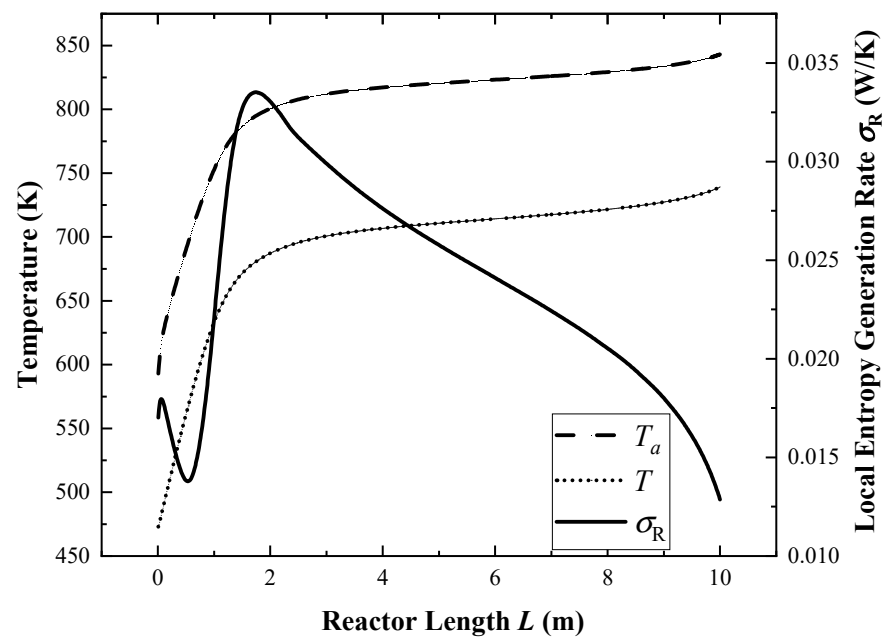
Figure 4. The distributions of T_a, T, and σ_R along the reactor.

In Figure 3, the ammonia decomposition reaction hardly occurs within the first 1 m of the reactor inlet section, and the permeation process has not yet occurred in the first 3 m, due to the low partial pressure of hydrogen in the reaction zone. With the progress of the reaction, the hydrogen partial pressure gradually increases, and the permeation process tends to be stable.

In Figure 4, the temperature in the first 1 m of the reactor rises rapidly. Because the temperature is low and the ammonia decomposition process does not occur at this stage, all the absorbed solar energy acts on the increase in gas temperature. After the temperature reaches about 630 K, the decomposition reaction starts to take place, which makes the temperature rise more and more slowly. After the reaction temperature reaches 690 K at 2 m, the temperature rises very slowly, and the reaction speed is at a stable level.

The local total entropy generation rate in Figure 4 shows a trend of increasing first, then decreasing, then rising to the highest peak, and finally continuing to decline. As the ammonia decomposition reaction has not yet occurred in the inlet section, the entropy generation rate is composed of heat transfer and pressure drop. The temperature difference between the outer wall and the reaction gas rapidly climbs from 120 K to 135 K, and then falls back to 120 K, resulting in an increase first and then a decrease in the heat transfer entropy generation rate. At the same time, both the pressure drop and flow velocity decrease continuously as the flow progresses, so the pressure drop entropy generation rate also decreases gradually. These two make the local entropy generation rate show the first peak at the inlet section of reactor. When it is close to 1 m, as the ammonia decomposition reaction rate increases rapidly with the increase in temperature, the entropy generation rate of the chemical reaction increases rapidly, so the total entropy generation rate rapidly climbs to the peak value. Then, with the gradual decrease in the temperature difference between the outer wall and the reaction gas from 120 K to 100 K, and the slow decrease in the chemical reaction rate, the local total entropy generation rate gradually decreases.

4.2. Three-Objective Optimization with the Heat Absorption Rate Constraint

Based on the performance analysis of Ref. [25], this paper further optimizes the parameters of the ammonia decomposition heat absorption system. In multi-objective optimization, the parameter optimization directions required by each performance index are often different, so there are contradictions between the four performance indicators. Meanwhile the heat absorption rate reflects the heat absorption capacity of the heat storage

reactor, which is the core performance index. Therefore, under the constraint of fixed heat absorption rate, three-objective optimization is carried out, that is, the irreversibility and efficiency of the system are optimized under the premise of ensuring acceptable core performance indicators.

The distribution of heat absorption rate is different under different light intensities. After trial calculation, when the light intensity is 600 W/m^2, 800 W/m^2, and 1000 W/m^2, the corresponding heat absorption rate benchmarks are 20.5 kW, 28.7 kW, and 36.8 kW. Under the condition that the actual heat absorption rate is not lower than the reference value at the corresponding light intensity, the three-objective optimization is carried out with the objectives of minimum entropy generation rate and the maximum thermal efficiency and energy conversion rate. The Pareto Front of the three-objective optimization at an illumination intensity of 800 W/m^2 is shown in Figure 5, and similar Pareto Front distributions are observed at 600 W/m^2 and 1000 W/m^2 light intensities.

Both the energy conversion rate and the entropy generation rate decrease with the increase in thermal efficiency. The entropy generation rate increases and the thermal efficiency decreases with the increase in the energy conversion rate. The thermal efficiency increases and the energy conversion rate decreases with the decrease in the entropy generation rate. This indicates that the minimum entropy generation rate and the maximum thermal efficiency have similar parameter optimization directions. The points in the Pareto Front thus exhibit a triangular surface distribution radiating from the point of lowest entropy generation rate and highest thermal efficiency.
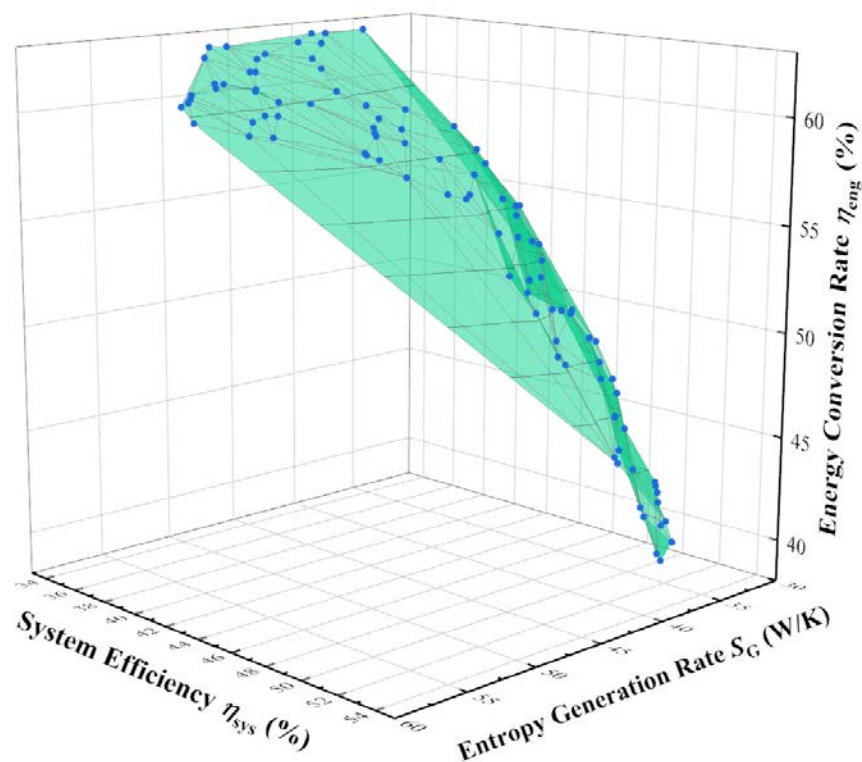

Figure 5. Pareto Front of three-objective optimization at 800 W/m^2.

Table 2 presents the performance indicators of the feature points on the Pareto Front when the light intensity is 800 W/m^2. When aiming at the highest energy conversion rate, the system will choose the highest ammonia preheat end-state temperature and the lowest permeation zone pressure, which can maximize the ammonia decomposition degree and improve the energy conversion rate from solar energy to chemical energy. Except for this situation, the system tends to choose the minimum to preheat the end-state temperature and moderate the permeation zone pressure. When aiming at the highest thermal efficiency,

the system will choose the largest flow rate and the smallest reactor radius to improve the heat absorption capacity and heat transfer performance. Except for this situation, the system prefers to choose a moderate flow rate and a larger reactor radius. Lastly, the reactor length is always about 10 m at all targets.

Table 2. Feature point parameters on the Pareto Front of three-objective optimization at 800 W/m^2.

System Parameters and Performance Indicators	Minimum $S_{G,SUM}$ Point	Maximum η_{sys} Point	Maximum η_{eng} Point	TOPSIS Decision Point
Ammonia gas preheating final temperature T_1 (K)	400	400	600	400
Ammonia molar flow rate N_A (mol/s)	0.52	0.8	0.61	0.5
Inner radius of membrane reactor R_2 (cm)	3.6	2.8	3.8	3.7
Reactor length L (m)	10.1	9.7	10.3	10
Osmotic zone pressure p_P (kPa)	54	55	10	45
Entropy generation rate S_G (W/K)	33.1	35.4	41.0	33.2
Thermal efficiency η_{sys} (%)	47.7	52.6	35.1	46.8
Energy conversion rate η_{eng} (%)	46.7	40.2	62.8	48.5

Compared with the reference system, the TOPSIS optimal system of three-objective optimization has a 4.8% decrease in entropy generation rate, a 1.5% increase in thermal efficiency, and a 1.4% increase in energy conversion rate. When the light intensity is 600 W/m^2, 800 W/m^2, and 1000 W/m^2, the optimal solutions obtained by the TOPSIS decision method are listed in Table 3. The greater light intensity matches the higher ammonia flow rate. This is consistent with the analysis in Ref. [25] that the ammonia flow rate should be matched with the light intensity to prevent the lower ammonia flow rate from being completely decomposed prematurely under larger light intensities.

Table 3. Parameters of TOPSIS optimal system in three-objective optimization under different light intensities.

System Parameters and Performance Indicators	600 W/m^2	800 W/m^2	1000 W/m^2
Ammonia gas preheating final temperature T_1 (K)	400	400	448
Ammonia molar flow rate N_A (mol/s)	0.31	0.5	0.6
Inner radius of membrane reactor R_2 (cm)	2.8	3.7	3.8
Reactor length L (m)	9.4	10	10
Osmotic zone pressure p_P (kPa)	35	45	47
Entropy generation rate S_G (W/K)	23.3	33.2	44.1
Thermal efficiency η_{sys} (%)	44.4	46.8	47.5
Energy conversion rate η_{eng} (%)	49.5	48.5	51.1

4.3. Four-Objective Optimization Releasing the Heat Absorption Rate Constraint

Based on Section 4.2, the heat absorption rate constraint is released, and the reactor parameters are optimized under different light intensities with objectives of maximum heat absorption rate, minimum entropy generation rate, maximum thermal efficiency, and maximum energy conversion rate. Figure 6 shows the Pareto Front when the light intensity is 800 W/m^2. Table 4 shows the feature point parameters on the Pareto Front at this time.
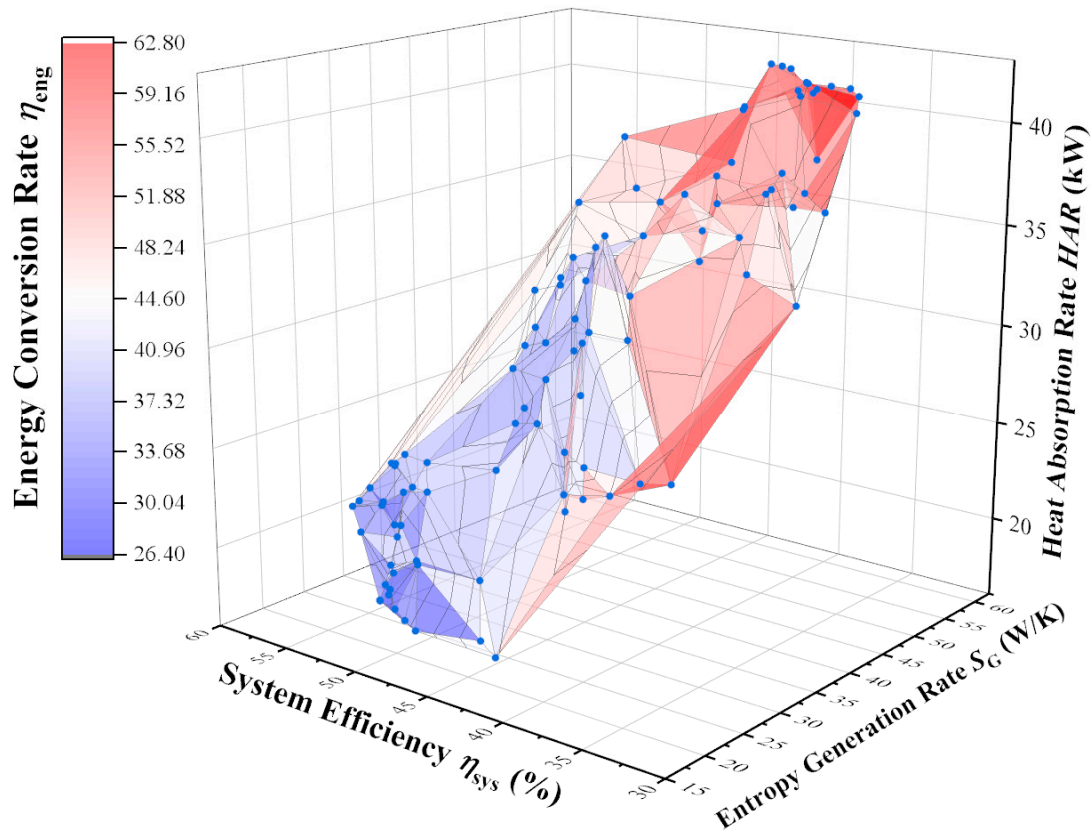
Figure 6. Pareto Front of four-objective optimization at 800 W/m^2.

Table 4. Feature point parameters on the Pareto Front of four-objective optimization at 800 W/m^2.

System Parameters and Performance Indicators	Maximum *HAR* Point	Minimum $S_{G,SUM}$ Point	Maximum η_{sys} Point	Maximum η_{eng} Point	TOPSIS Decision Point
Ammonia gas preheating final temperature T_1 (K)	400	400	400	600	400
Ammonia molar flow rate N_A (mol/s)	0.8	0.5	0.8	0.75	0.63
Inner radius of membrane reactor R_2 (cm)	2.8	3.8	2.8	3.8	3.8
Reactor length L (m)	13	7	7	12.8	7
Osmotic zone pressure p_P (kPa)	10	100	53	10	47
heat absorption rate *HAR* (kW)	42.4	17.6	21.2	40.8	20.7
Entropy generation rate S_G (W/K)	53.1	19.6	25.3	51.3	23.9
Thermal efficiency η_{sys} (%)	41.4	48.4	56.2	35.2	52.1
Energy conversion rate η_{eng} (%)	52.4	34.7	33.3	62.7	39.6

In Figure 6, the three-dimensional coordinate system is established based on three performance indicators of heat absorption rate, entropy generation rate, and thermal efficiency, and the color of the surface represents the energy conversion rate: the closer to blue, the lower the energy conversion rate, and the closer to red, the higher. From the distribution trend, with the increase in the heat absorption rate, the entropy generation rate and energy conversion rate increase, while the thermal efficiency decreases. With the increase in the thermal efficiency, the heat absorption rate, entropy generation rate, and energy conversion rate all decrease. With the increase in energy conversion rate, the heat

absorption rate and entropy generation rate increase, and the thermal efficiency decreases. These indicate that improving the thermal efficiency and reducing the entropy generation rate have similar optimization directions, while increasing the heat absorption rate and energy conversion rate have similar optimization directions.

Similar to the analysis of Table 2, the system still chooses the highest ammonia preheat end-state temperature and the lowest permeation zone pressure to improve the energy conversion rate. At the same time, due to the lower permeation zone pressure, more hydrogen is separated from the reactor, which increases the compressor power consumption and significantly decreases the thermal efficiency. When aiming at the highest heat absorption rate, the system will choose the lowest ammonia preheat end-state temperature, the highest ammonia flow rate, the smallest reactor radius, the longest reactor length, and the lowest permeation zone pressure, while the entropy generation rate of the system is extremely large.

Compared to the reference reactor, the TOPSIS decision point in Table 4 shows a 15.5% reduction in heat absorption rate, a 14% reduction in entropy generation rate, a 15.7% improvement in thermal efficiency, and an 8.7% reduction in energy conversion rate. Table 5 shows the parameters of the TOPSIS decision points under different light intensities.

Table 5. Parameters of TOPSIS optimal system in four-objective optimization under different light intensities.

System Parameters and Performance Indicators	600 W/m^2	800 W/m^2	1000 W/m^2
Ammonia gas preheating final temperature T_1 (K)	600	400	400
Ammonia molar flow rate N_A (mol/s)	0.3	0.63	0.6
Inner radius of membrane reactor R_2 (cm)	3.8	3.8	3.8
Reactor length L (m)	7	7	11.5
Osmotic zone pressure p_P (kPa)	10	47	76
heat absorption rate HAR (kW)	16.4	20.7	39.2
Entropy generation rate S_G (W/K)	19.4	23.9	43.7
Thermal efficiency η_{sys} (%)	33.7	52.1	48.0
Energy conversion rate η_{eng} (%)	62.3	39.6	46.1

5. Conclusions

Using FTT theory, a model of an ammonia decomposition solar heat absorption system based on the membrane reactor is established considering the ammonia decomposition membrane reactor, trough solar collector, regenerator, and compressor. The NSGA-II algorithm is applied to optimize the geometry and operating parameters of the system with the objectives of the highest heat absorption rate, the lowest entropy generation rate, the highest thermal efficiency, and the highest energy conversion rate. The main conclusions are as follows:

(1) In the four-objective optimization releasing the heat absorption rate constraint, the minimum entropy generation rate and the maximum thermal efficiency have similar optimization directions, while the maximum heat absorption rate and the maximum energy conversion rate have similar optimization directions.

(2) When aiming at the highest energy conversion rate, the system will select the highest ammonia preheat end-state temperature and the lowest permeation zone pressure. When aiming at the highest heat absorption rate, the system will choose the lowest ammonia preheat end-state temperature, the highest ammonia gas flow rate, the smallest reactor radius, the longest reactor length, and the lowest permeation zone pressure.

(3) In the three-objective optimization with the heat absorption rate constraint, the TOPSIS optimal system can reduce the entropy generation rate by 4.8% and increase the thermal efficiency and energy conversion rate by 1.5% and 1.4%, respectively.

(4)　In the four-objective optimization releasing the heat absorption rate constraint, the TOPSIS optimal system has a 15.5% reduction in heat absorption rate, a 14% reduction in entropy generation rate, a 15.7% increase in thermal efficiency, and an 8.7% decrease in energy conversion rate.

Author Contributions: Conceptualization, T.X. and S.X.; funding acquisition, S.X.; methodology, T.X., Q.J. and S.X.; software, Q.J. and T.X.; validation, S.X.; writing—original draft, T.X. and Q.J.; writing—review and editing, S.X. All authors have read and agreed to the published version of the manuscript.

Conflicts of Interest: The authors declare no conflict of interest.

References

1. Wang, D.L.; Zhang, C.; Yang, Y.; Zhang, L.; Bai, W.G.; Li, H.Z.; Yao, M.Y. Research progress of thermochemical energy storage system based on solar thermal power generation. *Therm. Power Gener.* **2019**, *48*, 1–9.
2. Wang, X.H.; Du, X.C.; Wei, J.J. Research progress of different solar thermochemical energy storage systems. *Chin. Sci. Bull.* **2017**, *62*, 3631–3642. [CrossRef]
3. Wu, J.; Long, X.F. Research progress of solar thermochemical energy storage. *Chem. Ind. Eng. Prog.* **2014**, *33*, 3238–3245. [CrossRef]
4. Lovegrove, K.M. Aspects of Thermochemical Storage and Transfer of Solar Energy Using Ammonia. Ph.D. Thesis, Australian National University, Canberra, Australia, 1992.
5. Luzzi, A. Solar Thermo-Catalytic Ammonia Dissociation. Ph.D. Thesis, Australian National University, Canberra, Australia, 1996.
6. Luzzi, A. High temperature solar tests with 1 kW chem ammonia reactor. *Fuel Energy Abstr.* **1995**, *36*, 271.
7. Luzzi, A.; Lovegrove, K.; Filippi, E.; Fricker, H.; Schmitz-Goeb, M.; Chandapillai, M.; Kaneff, S. Techno-economic analysis of a 10 MW solar thermal power plant using ammonia-based thermochemical energy storage. *Sol. Energy* **1999**, *66*, 91–101. [CrossRef]
8. Dunn, R.; Lovegrove, K.; Burgess, G. A review of ammonia-based thermochemical energy storage for concentrating solar power. *Proc. IEEE* **2012**, *100*, 391–400. [CrossRef]
9. Dunn, R.; Lovegrove, K.; Burgess, G.; Pye, J. An experimental study of ammonia receiver geometries for dish concentrators. *J. Sol. Energy Eng.* **2012**, *134*, 41007. [CrossRef]
10. Chuah, C.; Lee, J.; Bae, T. Graphene-based membranes for H_2 separation: Recent progress and future perspective. *Membranes* **2020**, *10*, 336. [CrossRef]
11. El-Attar, A.A.; El-Wakil, H.B.; Hassanin, A.H.; Bakr, B.A.; Almutairi, T.M.; Hagar, M.; Elwakil, B.H.; Olama, Z.A. Silver/Snail mucous PVA nanofibers: Electrospun synthesis and antibacterial and wound healing activities. *Membranes* **2022**, *12*, 536. [CrossRef]
12. Dalena, F.; Senatore, A.; Basile, M.; Knani, S.; Basile, A.; Iulianelli, A. Advances in methanol production and utilization, with particular emphasis toward hydrogen generation via membrane reactor technology. *Membranes* **2018**, *8*, 98. [CrossRef]
13. Itoh, N.; Oshima, A.; Suga, E.; Sato, T. Kinetic enhancement of ammonia decomposition as a chemical hydrogen carrier in palladium membrane reactor. *Catal. Today* **2014**, *236*, 70–76. [CrossRef]
14. Abashar, M.E.E.; Al-Sughair, Y.S.; Al-Mutaz, I.S. Investigation of low temperature decomposition of ammonia using spatially patterned catalytic membrane reactors. *Appl. Catal. A Gen.* **2002**, *236*, 35–53. [CrossRef]
15. Abashar, M. The impact of ammonia feed distribution on the performance of a fixed bed membrane reactor for ammonia decomposition to ultra-pure hydrogen. *Int. J. Hydrogen Energy* **2019**, *44*, 82–90. [CrossRef]
16. Wang, B.; Kong, H.; Wang, H.; Wang, Y.; Hu, X. Kinetic and thermodynamic analyses of mid/low-temperature ammonia decomposition in solar-driven hydrogen permeation membrane reactor. *Int. J. Hydrogen Energy* **2019**, *44*, 26874–26887. [CrossRef]
17. Cechetto, V.; Di Felice, L.; Medrano, J.A.; Makhloufi, C.; Zuniga, J.; Gallucci, F. H_2 production via ammonia decomposition in a catalytic membrane reactor. *Fuel Process. Technol.* **2021**, *216*, 106772. [CrossRef]
18. Sitar, R.; Shah, J.; Zhang, Z.; Wikoff, H.; Way, J.D.; Wolden, C.A. Compact ammonia reforming at low temperature using catalytic membrane reactors. *J. Membr. Sci.* **2022**, *644*, 120147. [CrossRef]
19. Cerrillo, J.L.; Morlanés, N.; Kulkarni, S.R.; Realpe, N.; Ramírez, A.; Katikaneni, S.P.; Paglieri, S.N.; Lee, K.; Harale, A.; Solami, B.; et al. High purity, self-sustained, pressurized hydrogen production from ammonia in a catalytic membrane reactor. *Chem. Eng. J.* **2022**, *431*, 134310. [CrossRef]
20. Chen, L.G.; Xia, S.J. Progresses in generalized thermodynamic dynamic-optimization of irreversible processes. *Sci. Sin. Technol.* **2019**, *49*, 981–1022.
21. Chen, L.G.; Xia, S.J.; Feng, H.J. Progresses in generalized thermodynamic dynamic-optimization of irreversible cycles. *Sci. Sin. Technol.* **2019**, *49*, 1223–1267.
22. Bejan, A. Notes on the history of the method of entropy generation minimization (finite time thermodynamics). *J. Non Equilib. Thermodyn.* **1996**, *21*, 239–242.

23. Andresen, B.; Berry, R.; Nitzan, A.; Salamon, P. Thermodynamics in finite time. I. The step-Carnot cycle. *Phys. Rev. A* **1977**, *15*, 2086–2093. [CrossRef]

24. Badescu, V. Optimal design and operation of ammonia decomposition reactors. *Int. J. Energy Res.* **2020**, *44*, 5360–5384. [CrossRef]

25. Xie, T.C.; Xia, S.J.; Kong, R.; Li, P.L.; Wang, C. Performance analysis of ammonia decomposition endothermic membrane reactor heated by trough solar collector. *Energy Rep.* **2022**, *8*, 526–538. [CrossRef]

26. Kong, R.; Chen, L.G.; Xia, S.J.; Zhang, L.; Feng, H.J. Minimization of entropy generation rate during hydrogen iodide decomposition reaction process. *Sci. Sin. Technol.* **2021**, *51*, 565–579. [CrossRef]

27. Kong, R.; Chen, L.; Xia, S.; Li, P.; Ge, Y. Minimization of Entropy Generation Rate in Hydrogen Iodide Decomposition Reactor Heated by High-Temperature Helium. *Entropy* **2021**, *23*, 82. [CrossRef]

28. Kong, R.; Chen, L.; Xia, S.; Li, P.; Ge, Y. Performance analysis of hydrogen iodide decomposition membrane reactor under different sweep modes. *Energy Convers. Manag.* **2021**, *244*, 114436. [CrossRef]

29. Xie, T.C.; Xia, S.J.; Wang, C. Multi-objective optimization of Braun-type exothermic reactor for ammonia synthesis. *Entropy* **2021**, *24*, 52. [CrossRef]

30. Wang, C.; Chen, L.G.; Xia, S.J.; Sun, F.R. Maximum production rate optimization for sulphuric acid decomposition process in tubular plug-flow reactor. *Energy* **2016**, *99*, 152–158. [CrossRef]

31. Sun, M.; Xia, S.J.; Chen, L.G.; Wang, C.; Tang, C.Q. Multi-objective optimization of sulfuric acid decomposition process using NSGA-II algorithm. *Energy Conserv.* **2020**, *39*, 118–123.

32. Li, P.L.; Chen, L.G.; Xia, S.J.; Zhang, L.; Kong, R.; Ge, Y.L.; Feng, H.J. Entropy generation rate minimization for steam methane reforming reactor heated by molten salt. *Energy Rep.* **2020**, *6*, 685–697. [CrossRef]

33. Li, P.L.; Chen, L.G.; Xia, S.J.; Zhang, L. Maximum hydrogen production rate optimization for tubular steam methane reforming reactor. *Int. J. Chem. React. Eng.* **2019**, *17*, 20180191. [CrossRef]

34. Li, P.L.; Chen, L.G.; Xia, S.J.; Kong, R.; Ge, Y.L. Total entropy generation rate minimization configuration of a membrane reactor of methanol synthesis via carbon dioxide hydrogenation. *Sci. China Technol. Sci.* **2022**, *65*, 657–678. [CrossRef]

35. Li, P.L.; Chen, L.G.; Xia, S.J.; Zhang, L. Entropy generation rate minimization for methanol synthesis via a CO_2 hydrogenation reactor. *Entropy* **2019**, *21*, 174. [CrossRef] [PubMed]

36. Xiong, Y.X.; Modibo, K.T.; Wu, Y.T.; Ma, C.F.; Zhang, Y.Q. Trough solar concentrating heat collection technology. *Sol. Energy* **2009**, 21–26.

37. Maansson, B.; Andresen, B. Optimal temperature profile for an ammonia reactor. *Ind. Eng. Chem. Process Des. Dev.* **1986**, *25*, 59–65. [CrossRef]

38. Hicks, R.E. Pressure Drop in Packed Beds of Spheres. *Ind. Eng. Chem. Fundam.* **1970**, *9*, 500–502. [CrossRef]

39. Li, Y.; Liao, S.; Gang, L. Thermo-economic multi-objective optimization for a solar-dish Brayton system using NSGA-II and decision making. *Int. J. Electr. Power Energy Syst.* **2015**, *64*, 167–175. [CrossRef]

40. Tian, Y.; Cheng, R.; Zhang, X.; Jin, Y. PlatEMO: A MATLAB platform for evolutionary multi-objective optimization [Educational Forum]. *IEEE Comput. Intell. Mag.* **2017**, *12*, 73–87. [CrossRef]

41. Yang, W.; Xu, K.; Lian, J.; Ma, C.; Bin, L. Integrated flood vulnerability assessment approach based on TOPSIS and Shannon entropy methods. *Ecol. Indic.* **2018**, *89*, 269–280. [CrossRef]

42. Shih, H.S.; Shyur, H.J.; Lee, E.S. An extension of TOPSIS for group decision making. *Math. Comput. Model.* **2007**, *45*, 801–813. [CrossRef]